This is a pre-print version of the paper. Please cite the final version of the paper:

G. Di Martino, A. Di Simone, A. Iodice and D. Riccio, “Scattering-Based Nonlocal Means SAR Despeckling”, *IEEE Trans. Geosci. Remote Sens.*, vol. 54, no. 6, pp. 3574-3588, June 2016. DOI: 10.1109/TGRS.2016.2520309.

Scattering-Based Nonlocal Means SAR Despeckling

Gerardo Di Martino, *Member, IEEE*, Alessio Di Simone, Antonio Iodice, *Senior Member, IEEE*, and Daniele Riccio, *Fellow, IEEE*

***Abstract*—Speckle noise greatly limits both synthetic aperture radar (SAR) data human readability, especially for non-SAR-expert users, and performance of automatic processing and information retrieval procedures by computer programs. Therefore, despeckling of SAR images is an essential preprocessing step in SAR data analysis, processing, and modeling, as well as in information retrieval and inversion procedures. Up to now, one of the most accurate and promising despeckling approaches—among those based on a single SAR image—is the one relying on the nonlocal means concepts. However, at the best of our knowledge, most of the state of the art considers the despeckling problem only within a statistical framework, completely discarding the electromagnetic phenomena behind SAR imagery formation. In this paper, we introduce the novel idea of a physical-based despeckling, taking into account meaningful physical characteristics of the imaged scenes. This idea is realized via the implementation of a physical-oriented probabilistic patch-based (PPB) filter based on *a priori* knowledge of the underlying topography and analytical scattering models. This filter is suitable for SAR images of natural scenes presenting a significant topography. An adaptive version of the proposed scattering-based PPB filter for denoising of SAR images including both mountainous and flat areas is also developed. The performances of the proposed filter and its adaptive version are evaluated both qualitatively and quantitatively in numerical experiments using both simulated and actual SAR images. The proposed technique exhibits performance superior w.r.t. the standard PPB filter and comparable or, in some cases, superior to the state of the art, both in terms of speckle reduction and texture and detail preservation.**

***Index Terms*—Fractals, image denoising, nonlocal means (NLM), scattering models, synthetic aperture radar (SAR).**

I. Introduction

SYNTHETIC aperture radar (SAR) data represent an essential tool for monitoring Earth resources and analyzing both urban and natural areas. As the very recent European Space Agency Sentinel mission shows, SAR systems and sensors play a key role in understanding, controlling, and preserving our surrounding environment. However, SAR image readability and information retrieval procedures are dramatically affected by speckle, the multiplicative noise typical of SAR coherent acquisition systems. Consequently, analysis and understanding of a single-look SAR image are often a difficult task even for SAR-expert users [1]. In the last decades, with the introduction of increasingly powerful hardware and software resources, huge efforts have been made in the despeckling field, aimed at the reduction of speckle effects to increase the readability of SAR data and, consequently, the number of non-SAR-expert users approaching SAR imagery.

Numerous kinds of approaches and methods facing the despeckling problem have been proposed so far, as it can be appreciated from the surveys that can be found in [2]–[4]. The first technique is the so-called spatial multilook, simply based on an incoherent averaging of neighboring pixels within a fixed window. Despite its simplicity, this technique is the best (with respect the mean-squared error) in the case of homogenous SAR images, i.e., SAR images of surfaces with constant geometrical and electromagnetic parameters. Unluckily, in most cases, a homogenous SAR image is not of practical interest, and it is of really rare occurrence. Typically, SAR images depict a very inhomogeneous scenario, i.e., regions characterized by spatial variations of at least one of the numerous parameters influencing SAR image formation (dielectric constant, electrical conductivity, and microscopic and macroscopic roughness). Depending on these parameter variations, SAR images present several features like edges—typically associated with changes of the electromagnetic parameters of the surface—textures and patterns—typically associated with changes of the geometric parameters of the surface—homogenous regions, and so on. The huge amount of information carried by these features makes their preservation of key importance in despeckling.

Seeking inspiration from the huge literature about denoising of signals affected by the additive white Gaussian noise (AWGN) and of the well-assessed related techniques has been, for a long time, the most followed approach in the development of despeckling algorithms for SAR images: as a matter of fact, numerous both old and recent techniques used the homomorphic approach, taking the logarithm of the data [5]–[7]. Despite their simplicity and analytical tractability, the homomorphic approach causes a severe distortion of the dynamics, as well as of the fundamental properties of the SAR data. In fact, the log-transformed speckle noise is neither Gaussian nor zero-mean so that AWGN denoising methods would not provide reliable results unless these noise peculiarities are properly taken into account. As soon as speckle statistical descriptions and models became available in literature [8], [9] and the denoising community became more aware about the peculiarities of SAR images [10], e.g., spatial nonstationarity, more advanced techniques were conceived and developed [11]–[19].

As an alternative to the previous techniques, all operating in the native data domain, i.e., the spatial one, the 1990s saw the rapid diffusion of the wavelet-based denoising techniques [7], [20]–[23]. This approach allows for both huge noise reduction

Manuscript received August 11, 2015; revised November 7, 2015; accepted January 15, 2016.

The authors are with the Dipartimento di Ingegneria Elettrica e delle Tecnologie dell'Informazione, Università di Napoli Federico II, 80125 Naples, Italy (e-mail: gerardo.dimartino@unina.it; alessio.disimone@unina.it; iodice@unina.it; daniele.riccio@unina.it).

Color versions of one or more of the figures in this paper are available online at http://ieeexplore.ieee.org.

Digital Object Identifier 10.1109/TGRS.2016.2520309

and detail preservation, owing to the sparse representation of the signal in the transformed domain. Wavelet transform ensures a very accurate separation between signal and noise, also with richly detailed images, so that excellent and promising results are provided by wavelet-based approaches.

More recently, the nonlocal means (NLM) approach, first introduced in [24], has been developed, and it represents a candidate breakthrough in the despeckling community. The basic idea is to provide an estimate of the clean image via a proper averaging of similar pixels or patches, i.e., blocks of close pixels. The main contribution is to introduce, in a very basic way, some physical concepts by means of an intensity-based similarity criterion rather than of a pure geometrical one. NLM techniques are actually of great interest, owing to their edge preservation and speckle reduction capabilities [23]–[25]. The nonlocal filter proposed in [24], optimal for AWGN, was generalized to SAR imagery and speckle noise by Deledalle *et al.* in [25], introducing a distance suitable for the Nakagami–Rayleigh distribution typical of SAR speckle noise. An improved version of the filter in [25] suitable for both polarimetric and interferometric SAR data has been published very recently [26].

Despite their peculiarities, all of the aforementioned approaches suffer a general lack of physically based concepts: despeckling is considered as a pure statistical estimation problem, without taking into account the physical phenomenology inherent to the SAR image acquisition process. However, electromagnetic scattering phenomena play a key role in the SAR image formation process: SAR data can be modeled as the reflectivity pattern of the illuminated scene filtered by the SAR system [27], [28]. The past and current representation-based approaches in denoising SAR images could be substituted by the more meaningful and promising object-based approach, in which the similarity criterion is evaluated on the object properties rather than on those of its representation through the sensor. However, an object-based approach cannot be performed without taking into account the physics behind the data acquisition and the related phenomena, which, in the SAR case, are essentially represented by scattering. In the meantime, the availability of both closed-form scattering models—as the geometrical optics, physical optics (PO), integral equation methods, and small-perturbation method (SPM) [29]–[31]—and a more accurate knowledge of all those parameters and phenomena involved in electromagnetic scattering from natural surfaces call for the introduction of scattering concepts in despeckling in order to obtain a significant improvement of the state of the art.

In this paper, we introduce the novel idea of despeckling based on scattering phenomena hidden behind SAR image formation. In [32], we made a first naïve but promising attempt in this direction by adding a similarity criterion simply based on local incidence angle to the intensity-based one. Here, in a more rigorous way, we apply this general idea to the probabilistic patch-based (PPB) filter proposed in [25] by employing a scattering-based similarity criterion. In particular, we select the electromagnetic scattering model suitable to natural surfaces, and then, we modify the PPB filter, introducing scattering concepts in the definition of the filter weights as a kind of *a priori* knowledge, in order to take into account the electromagnetic behavior of the scattering cell. We call this new filter scattering-based PPB (SB-PPB) filter. The proposed approach requires the knowledge of the scene topography. As discussed more in detail later, this does not significantly limit the applicability of the method since accurate digital elevation models (DEMs) are by now easily available for most part of the world.

This paper is organized as follows. Section II describes the state of the art of NLM despeckling techniques, with a particular emphasis on the PPB filter. Section III presents the direct model used in the proposed filter. In Section IV, we present the rationale and the implementation details of the proposed NLM filter and of its adaptive version. Its performances are assessed in a qualitative and quantitative way, applying the proposed SB-PPB filter to both simulated and actual SAR images in Section V. Some conclusion and recommendations close this paper.

II. Related Works and Motivations

Up to now, NLM represents one of the most widespread, accurate, and promising approaches to SAR imagery despeckling [3], [4], [23], [25], [33]. At a very basic level, the main idea of despeckling is essentially to average *similar objects*: most of the denoising algorithms and approaches can be comprised within these two words. Different similarity criteria and/or different averages of the objects give rise to very different techniques. The basic idea of the nonlocal approach is very intuitive, but it represented a total breakthrough in the denoising community: similarity is no more intended in a pure and exclusive geometrical sense. The geometric Euclidean distance was substituted by the more meaningful intensity distance aimed at averaging only those objects sharing the same physical properties, i.e., the reflectivity. In other words, only those pixels presenting similar amplitude values are averaged, irrespective of their geometric distance. The more similar two pixels are, the greater the weight assigned to them in the average process. The Euclidean intensity distance first proposed by Buades *et al.* in [24] was designed and derived in the assumption of AWGN. This distance was recently modified by Deledalle *et al.* in [25] to account for the special characteristics of SAR speckle noise.

In the 1980s, the sigma filter for additive signal-independent noise [34] and its extension to speckle noise [35] pioneered the application of NLM concepts. Nowadays, PPB [25] and SAR block-matching 3-D (SAR-BM3D) [23] filters can be arguably considered the state of the art for SAR imagery denoising. In particular, SAR-BM3D [23] collects together several of the most advanced concepts in denoising—block-matching, nonlocal filtering, wavelet shrinkage, and Wiener filtering—first proposed by Dabov *et al.* in [36], in a way suitable for SAR image peculiarities. The algorithm is a two-step procedure: the first step provides a gross estimate of the clean image that is used as input of the second step in which a Wiener filtering is applied to the noisy image in order to provide the final despeckled image. Block matching and nonlocal filtering are performed via a similarity criterion suitable for SAR speckle peculiarities. The distance used to evaluate the block similarity is that developed in [25].

These patch-based nonlocal algorithms very often show better results w.r.t. other methods [3], [4], [23], [25], [33], although they present some limitations and difficulties in very specific cases, especially for small nonrepetitive features, due to the failure of the patch-matching step.

A detailed description of the PPB filter, on which the proposed SB-PPB filter is based, is reported in the following. In their original work, Deledalle *et al.* [25] proposed a probabilistic approach for filter weight evaluation based on the weighted maximum likelihood estimation (WMLE). The image denoising problem consists in finding the best estimate of the parameter of the parametric noise distribution $p(A_s|\sigma_s)$, with A_s being the amplitude sample located in s and σ_s being a space-varying unknown parameter, assumed to be the reflectivity [i.e., the normalized radar cross section (NRCS)] of the scene at pixel s (so that the noise-free amplitude A_s^* is the square root of σ_s). In [25], it was shown that, if the pixel amplitudes are modeled as independent and identically distributed according to the Nakagami–Rayleigh distribution [10], in agreement with the usual multiplicative speckle noise description, then the WMLE of σ_s can be expressed as

$$\hat{\sigma}_s^{\mathrm{WMLE}} = \frac{\sum_{t\in\Omega} w_{s,t} A_t^2}{\sum_{t\in\Omega} w_{s,t}} \tag{1}$$

where Ω is a (large) window centered at s (*search window*) and the weight $w_{s,t} \in [0,1]$ depends on the target pixel s and the test pixel t; it can be also seen as a measure of the similarity between the two pixels. The definition of the weights is the key-point of the NLM techniques, as they are directly related to the accuracy of the algorithm. In order to take into account the neighborhood of the pixel under study, in [25], the patch concept is introduced, and the weight is evaluated as the probability that the two patches Δs and Δt, centered at s and t, respectively, share the same parameters

$$w_{s,t}^{\mathrm{non-it.\ PPB}} \triangleq p(\sigma_{\Delta s} = \sigma_{\Delta t}|A)^{\frac{1}{h}} \tag{2}$$

where $h > 0$ is a filter parameter setting the weight decay and the superscript "non-it. PPB" stands for noniterative PPB.

In order to refine the weights, Deledalle *et al.* [25] proposed also an iterative scheme in which the reflectivity estimation at step $i-1$ $\hat{\sigma}^{i-1}$ is used as a kind of *a priori* knowledge at step i

$$w_{s,t}^{\mathrm{it.\ PPB},i} \triangleq p\left(\sigma_{\Delta s} = \sigma_{\Delta t}|A, \hat{\sigma}^{i-1}\right)^{\frac{1}{h}} \tag{3}$$

with the obvious meaning of the superscript "it. PPB." In addition, using again the Nakagami–Rayleigh distribution for modeling the speckle noise and the Kullback–Leibler divergence for modeling the *a priori* knowledge, the following weight expression can be derived [25]:

$$w_{s,t}^{\mathrm{it.\ PPB},i} = \exp\left[-\sum_k \left(\frac{1}{\tilde{h}} \ln\left(\frac{A_{s,k}}{A_{t,k}} + \frac{A_{t,k}}{A_{s,k}}\right) + \frac{L}{T_{\mathrm{fil}}} \frac{\left|\hat{\sigma}_{s,k}^{i-1} - \hat{\sigma}_{t,k}^{i-1}\right|^2}{\hat{\sigma}_{s,k}^{i-1}\hat{\sigma}_{t,k}^{i-1}}\right)\right] \tag{4}$$

where L stands for the equivalent number of looks, $\tilde{h} = h/(2L-1)$, T_{fil} is a filter parameter dictating the decay of the Kullback–Leibler divergence, and k is an index that identifies the pixels within patches Δs and Δt, so that, for instance, $A_{s,k}$ is the amplitude of the kth pixel of the patch Δs. The logarithmic term in (4) weights in an optimal way (in the framework of an MLE approach) the observed amplitude image samples via a distance suitable for SAR data, whereas the second term takes into account the previous estimate in an iterative scheme and is aimed at avoiding filtering samples drawn from different distributions. For $T_{\mathrm{fil}} \to \infty$, we have the noniterative version of the algorithm, for which

$$w_{s,t}^{\mathrm{non-it.\ PPB}} = \exp\left[-\sum_k \frac{1}{\tilde{h}} \ln\left(\frac{A_{s,k}}{A_{t,k}} + \frac{A_{t,k}}{A_{s,k}}\right)\right]. \tag{5}$$

Since a complete description of the PPB filter goes outside the scope of this paper, the reader is referred to [25] for more details. In the next section, we present the scattering model used in the proposed SB-PPB filter.

III. Scattering Model

In this section, the electromagnetic scattering model for natural surfaces used for the development of the filter is presented. The proposed direct model is divided in two parts: first, the natural surface under study is properly modeled using fractal geometry; in particular, a fractional Brownian motion (fBm) is used. To cope with the nondifferentiability of the fBm process and the limited range of fractalness of natural surfaces, a smoothed version of the original fBm process must be introduced (*physical fBm*) [29].

The second step consists in adopting a scattering model, i.e., a method for the evaluation of the field scattered from the previously modeled natural surface. In this step, a relationship between the backscattering coefficient and the geometrical (in particular, local incidence angle) and electromagnetic parameters of the surface is derived.

A. Surface Model

Many surface models have been presented in the scientific literature—deterministic, stochastic, and empirical—each with its advantages and drawbacks. Among these, the most accepted and suitable model for natural surfaces is the fractal one [29], [37]–[39]. One of the reasons for this success stands in the ability of fractal models to properly account for the statistical scale-invariance properties (in particular, self-affinity) of natural surfaces. Analytic models reported here are able to handle a variety of natural surfaces: bare and moderately vegetated soils, as well as ocean surfaces. In particular, we consider here a (topological) 2-D fBm stochastic process $z(x,y)$ defined as follows [29]:

$$\Pr\left\{z(x,y) - z(x',y') < \bar{\zeta}\right\} = \frac{1}{\sqrt{2\pi}T^{1-H}\tau^H} \int_{-\infty}^{\bar{\zeta}} \exp\left(-\frac{\zeta^2}{2T^{2(1-H)}\tau^{2H}}\right) d\zeta \tag{6}$$

where $\Pr\{\}$ stands for "probability," $\bar{\zeta}$ is the considered height increment, $z(x,y)$ is the surface elevation

$$\tau = \sqrt{(x-x')^2 + (y-y')^2} \tag{7}$$

is the distance between the two considered points of coordinates (x, y) and (x', y'), and

- H: Hurst coefficient $(0 < H < 1)$ related to the fractal dimension $D = 3 - H$;
- T: topothesy [m], i.e., the distance over which chords joining points on the surface have a root mean square slope equal to unity.

Fractal geometry is the mathematical abstraction of fractal physics: fractal surfaces exhibit properties (for instance, self-affinity) at all scales, and they are not differentiable at any point. Surface random fractal corrugations possess power spectra that diverge in the low-frequency regime (infrared catastrophe) and exhibit nonstationary correlation functions. Use of the mathematical fractals to model natural surfaces would make any scattering computation completely intractable [29]. However, natural surfaces are observed, sensed, measured, and represented via instruments that are, for their intrinsic nature, band-limited. In other words, no actual natural surface holds property (6) at any scale, and some properties of fBm mathematical surfaces may be relaxed. Accordingly, the mathematical fractals may be band-limited, thus generating the physical fractals that hold most of the properties needed to manage them in the electromagnetic scattering theory. In particular, the range of scales of interest for a scattering problem is limited, on one side, by the finite linear size of the illuminated surface and, on the other side, by the fact that surface variations on scales much smaller than the incident wavelength λ do not affect the scattered field. An efficient approach of surface modeling relies on considering surfaces that satisfy property (6) only in a limited range of τ [29]. That is why these surfaces are also referred to as *band-limited fBm* or *physical fBm*, as defined in [29]. It is noteworthy that actual natural surfaces exhibit typical values of H between 0.5 and 0.9 as reported in related literature [40]–[45].

B. Scattering Model

The second step of the direct model consists in the choice of the electromagnetic method, i.e., the scattering model. In general, no analytical closed-form exact solution for the scattered field is achievable for natural surfaces. Only approximate analytical solutions are obtained by making simplifying assumptions for the boundary conditions relevant to the scattering surface; different approximations lead to different methods to evaluate the scattered field, and each method holds under the appropriate surface roughness regime and illumination conditions.

Two main frameworks allow for closed-form solutions to the scattering problem [29]. One is referred to as the Kirchhoff approximation (KA) and leads to the PO solution. The other one is the extended-boundary-condition method, which leads to the SPM. In this paper, we select the SPM because it provides the simplest expression for the NRCS and shows a range of validity often adequate to SAR applications. Thus, this method provides a very simple relation between fractal parameters and backscattered field.

Considering a monostatic radar and assuming that the surface can be described as a physical fBm, the SPM estimation $\hat{\sigma}^{\mathrm{SPM}}$ of the NRCS σ is given by [46], [47]

$$\hat{\sigma}^{\mathrm{SPM}} = 2\pi 8 k^4 S_0 |\beta_{mn}|^2 \frac{\cos^4\theta}{(2k\sin\theta)^{2+2H}} \tag{8}$$

wherein m and n denote the transmitted and received polarizations, respectively, and may stand for *horizontal* or *vertical* polarization; k is the electromagnetic wavenumber of the incident field; S_0 is a parameter characterizing the spectral behavior of the physical fBm surface, expressed in $[\mathrm{m}^{-2-2H}]$, and related to T and H [29]; and β_{mn}, accounting for the incident and reflected field polarization, is a function of both the complex relative dielectric constant of the surface and the local incidence angle θ, i.e., the angle between the propagation direction of the incoming radar electromagnetic wave and the direction orthogonal to the local mean plane approximating the resolution cell [29]. Note that, according to this model, $\beta_{mn} = 0$ for $m \neq n$ so that SPM is able to deal only with the copolarized case; however, a nonnull closed-form expression of the NRCS for the cross-polarized case can be still obtained, extending the SPM by using the polarimetric two-scale model, described in [48]. From now on, the subscripts related to the polarization will be neglected. Equation (8) describes the NRCS of a single resolution cell with a microscopic roughness described by the fractal parameters H and T (or H and S_0) and with a macroscopic roughness described by the local incidence angle θ.

In the next section, the method proposed to introduce the scattering model in the despeckling process is presented.

IV. Scattering-Based NLM

Following the approach in [25], the nonlocal filter output is computed according to (1), and the filter weights are defined as the probability that the NRCSs of the two patches Δs and Δt are equal given an appropriate *a priori* knowledge. In particular, we introduce the scattering behavior of the resolution cell as an *a priori* knowledge. Accordingly, the following filter weight definition is proposed:

$$w_{s,t}^{\text{non-it. SB-PPB}} \triangleq p\left(\sigma_{\Delta s} = \sigma_{\Delta t} | A, \hat{\sigma}^{\mathrm{SPM}}\right)^{\frac{1}{h}} \tag{9}$$

with $\sigma_{\Delta s}$ and $\sigma_{\Delta t}$ being the NRCS in the selected (Δs) and test (Δt) patch and A being the amplitude SAR signal; $\hat{\sigma}^{\mathrm{SPM}}$ takes into account the *a priori* information about the signal backscattered from the scene, and h is a parameter controlling the weight decay. By proceeding in a way similar to that of [25], we have

$$\begin{aligned} w_{s,t}^{\text{non-it. SB-PPB}} &= \exp\left[-\frac{2L-1}{h}\sum_k \ln\left(\frac{A_{s,k}}{A_{t,k}} + \frac{A_{t,k}}{A_{s,k}}\right) \right. \\ &\qquad \left. + \frac{1}{h}\sum_k \ln p\left(\sigma_{s,k} = \sigma_{t,k} | \hat{\sigma}^{\mathrm{SPM}}\right)\right] \\ &= w_{s,t}^{\text{non-it. PPB}} \exp\left[\frac{1}{h}\sum_k \ln p\left(\sigma_{s,k} = \sigma_{t,k} | \hat{\sigma}^{\mathrm{SPM}}\right)\right]. \end{aligned} \tag{10}$$

Therefore, to properly take into account scattering, a description of the *a priori* probability $p(\sigma_{s,k} = \sigma_{t,k} | \hat{\sigma}^{\mathrm{SPM}})$ is required.

To this aim, we use the approach proposed in [25], thus modeling the *a priori* term via the symmetric version of the Kullback–Leibler divergence [25]

$$\begin{aligned} & p\left(\sigma_{s,k}=\sigma_{t,k}|\hat{\sigma}^{\mathrm{SPM}}\right) \\ & \quad \propto \exp\left\{-\frac{1}{T_{\mathrm{fil}}}\int\left[p\left(\sigma|\hat{\sigma}_{s,k}^{\mathrm{SPM}}\right)\right.\right. \\ & \qquad \left.\left.-p\left(\sigma|\hat{\sigma}_{t,k}^{\mathrm{SPM}}\right)\right]\ln\frac{p\left(\sigma|\hat{\sigma}_{s,k}^{\mathrm{SPM}}\right)}{p\left(\sigma|\hat{\sigma}_{t,k}^{\mathrm{SPM}}\right)}d\sigma\right\} \\ & \quad \propto \exp\left(-L\frac{\left|\hat{\sigma}_{s,k}^{\mathrm{SPM}}-\hat{\sigma}_{t,k}^{\mathrm{SPM}}\right|^2}{\hat{\sigma}_{s,k}^{\mathrm{SPM}}\hat{\sigma}_{t,k}^{\mathrm{SPM}}}\right). \end{aligned} \tag{11}$$

As a consequence

$$\begin{aligned} & w_{s,t}^{\text{non-it. SB-PPB}} \\ & \quad = \exp\left[-\sum_k\left(\frac{1}{\tilde{h}}\ln\left(\frac{A_{s,k}}{A_{t,k}}+\frac{A_{t,k}}{A_{s,k}}\right)\right.\right. \\ & \qquad \left.\left.+\frac{L}{T_{\mathrm{fil}}}\frac{\left|\hat{\sigma}_{s,k}^{\mathrm{SPM}}-\hat{\sigma}_{t,k}^{\mathrm{SPM}}\right|^2}{\hat{\sigma}_{s,k}^{\mathrm{SPM}}\hat{\sigma}_{t,k}^{\mathrm{SPM}}}\right)\right] \\ & \quad = w_{s,t}^{\text{non-it. PPB}}\cdot\exp\left(-\sum_k\frac{L}{T_{\mathrm{fil}}}\frac{\left|\hat{\sigma}_{s,k}^{\mathrm{SPM}}-\hat{\sigma}_{t,k}^{\mathrm{SPM}}\right|^2}{\hat{\sigma}_{s,k}^{\mathrm{SPM}}\hat{\sigma}_{t,k}^{\mathrm{SPM}}}\right). \end{aligned} \tag{12}$$

Note that this equation is formally identical to (4), provided that the σ estimation at previous step $\hat{\sigma}^{i-1}$ is replaced by the σ value computed by the scattering model $\hat{\sigma}^{\mathrm{SPM}}$. It is also worth noticing that (12) reduces to (5), i.e., to usual noniterative PPB, for flat areas, because in this case $\hat{\sigma}_{s,k}^{\mathrm{SPM}}=\hat{\sigma}_{t,k}^{\mathrm{SPM}}$, so that $w_{s,t}^{\text{non-it. SB-PPB}}=w_{s,t}^{\text{non-it. PPB}}$.

Evaluation of (12) via the expression (8) requires the availability of a DEM of the sensed surface, so that the local incidence angle can be computed, and knowledge of the terrain complex relative dielectric constant, Hurst parameter, and spectral parameter. However, if the underlying topography is significant, the backscattered signal and, hence, SAR intensity variations are mostly due to the topographic content of the sensed surface, due to the major influence of the local incidence angle on the NRCS with respect to the remaining parameters (see the sensitivity analysis reported in the Appendix). Accordingly, we can reasonably assume that S_0 is constant in the search window, so that it cancels out in (12); in addition, dependence on ε_r can be neglected, and a standard ε_r value can be used in (8), so that we can assume

$$\hat{\sigma}_p^{\mathrm{SPM}}=\hat{\sigma}^{\mathrm{SPM}}(\theta_p)\propto|\beta(\theta_p)|^2\frac{\cos^4\theta_p}{(\sin\theta_p)^{2+2H}} \tag{13}$$

where θ_p is the local incidence angle evaluated in the location p. With regard to the Hurst coefficient H, it can be estimated from the SAR image via the algorithm by Di Martino *et al.* [28], if one assumes that the same value of H holds at both macroscopic and microscopic scales. This is a rather strong assumption, but again, the sensitivity analysis in the Appendix shows that errors on the value of H do not appreciably affect scattering evaluation if a significant topography is present. Accordingly, in conclusion, evaluation of the weight (12) only requires availability of the scene DEM. We want to underline that this does not significantly limit the applicability of our method since accurate DEMs are by now easily available for most part of the world, often free of charge. In fact, the Shuttle Radar Topography Mission [49] provided a DEM of the entire Earth (with the exception of polar areas), freely available at [50]. In addition, lidar data providing very high resolution DEMs are becoming more and more widespread, especially in the most developed countries. For instance, the DEM employed in our work (Section V-C) is publicly available at no cost at the Naples (Italy) local authority website [51].

Finally, it must be noted that the employed fractal direct model (13) describes single bounce scattering phenomena typical of many natural scenarios (rocks, geomorphologic relief, bare, or little vegetated soil). It does not describe other phenomena, such as volume scattering (e.g., from vegetation), and layover, shadowing and double bounce effects, typical of urban and suburban areas. In addition, as already mentioned, a uniform standard value of ε_r is assumed. However, this does not mean that the proposed filter is not applicable to different scenarios, where the scattering model is not accurate or ε_r is space-varying. In fact, together with the new distance term based on scattering, the weight used by our algorithm still retains the PPB distance term based on intensity [see (5) and (12)], owing to which SB-PPB can be expected to work well also in regions in which the employed scattering model is not accurate. Further help with this regard is expected to be provided by the adoption of an adaptive scheme, as described in the following. The aforementioned expectations are confirmed by the experimental results of Section V.

A. Adaptive Scheme

In order to fill the lack of a proper nonuniform *a priori* knowledge in the initial estimate, Deledalle *et al.* proposed also an iterative scheme within the PPB filter [25], with refined weights given by (4) (see Section II). Iterations ensure a better preservation of edges and texture. It is then meaningful to discuss the use of this iterative scheme also for the proposed SB-PPB filter. It is noteworthy that, whenever topography represents the main contribution to the backscattering variations over the scene, an iterative scheme of the proposed technique does not provide relevant improvements since gray-level variations of the SAR image are already properly taken into account by the *a priori* knowledge about the local incidence angle (see Section V for an experimental verification). Nevertheless, in case of scenes presenting gentle topography and SAR image intensity variations not related to topography (i.e., related to variations of scene electromagnetic parameters, microscopic roughness or scattering phenomena not described by the proposed one, e.g., volume scattering typical of vegetated areas and double bounce, layover, and shadowing typical of urban areas),

iterations can provide better edge and feature preservation capabilities w.r.t. the noniterative version. In a realistic scenario, distinguishing the main source of the SAR intensity variations may not be an easy task. However, if a DEM of the sensed surface is available, it is possible to establish if the local topography is significant or not. Following this idea, we propose a simple flat—nonflat binary classification-based adaptive iterative scheme of the proposed filter, based on the iterative PPB filter presented in [25]. Iterations are adaptively performed only in those regions characterized by a flat topography.

B. Filter Rationale

The rationale of the proposed adaptive SB-PPB filter is presented in the following. From the DEM of the sensed scene, the local incidence angle map can be easily computed as follows [28]:

$$\theta = \cos^{-1}\left(\frac{p\sin\theta_0 + \cos\theta_0}{\sqrt{p^2+q^2+1}}\right) \tag{14}$$

where θ_0 is the radar look angle (i.e., the incidence angle over an horizontal surface) and p and q are the range and azimuth slopes, respectively, i.e., $p = \partial z/\partial y$, and $q = \partial z/\partial x$, with z being the elevation map. In order to insert the *a priori* knowledge in the proposed filter, the local incidence angle map has to be projected into the SAR system geometry and coregistered to the noisy SAR image. This step is by now standard in SAR processing, and it can be easily performed by most of the available commercial software tools. The local incidence angle map is then divided in fixed-size blocks: each block undergoes a binary flat–nonflat classification process. A block is classified as flat if the standard deviation of the local incidence angle is less than a fixed threshold. SAR image blocks corresponding to nonflat regions undergo the noniterative scheme of the proposed filter, i.e., filter weights defined by (12) are used. This corresponds to applying the PPB filter as introduced in [25] with a proper initial estimate provided by (13), in which the incidence angle computed via (14) is inserted. Conversely, in SAR image blocks corresponding to flat regions, the iterative scheme is employed, in order to refine weights in regions with nontopographic-related SAR intensity variations, such as edges, man-made features, etc., and improve the edge and feature preservation capability of the filter. In this case, after the first iteration, the *a priori* knowledge about topography is no more used, and it is substituted by the previous intensity estimate, exactly as in [25], i.e., the weights defined in (4) are used. The flowchart of the algorithm is shown in Fig. 1. Finally, it is worth noticing that, apart from the H estimation and coregistration steps, whose computing time requirements are analyzed in the following sections, the adaptive SB-PPB filter has a complexity comparable to that of the PPB filter, the execution time depending on the flatness of the analyzed surface. In particular, the adaptive scheme allows for time saving in nonflat regions w.r.t. the iterative PPB, avoiding further iterations.

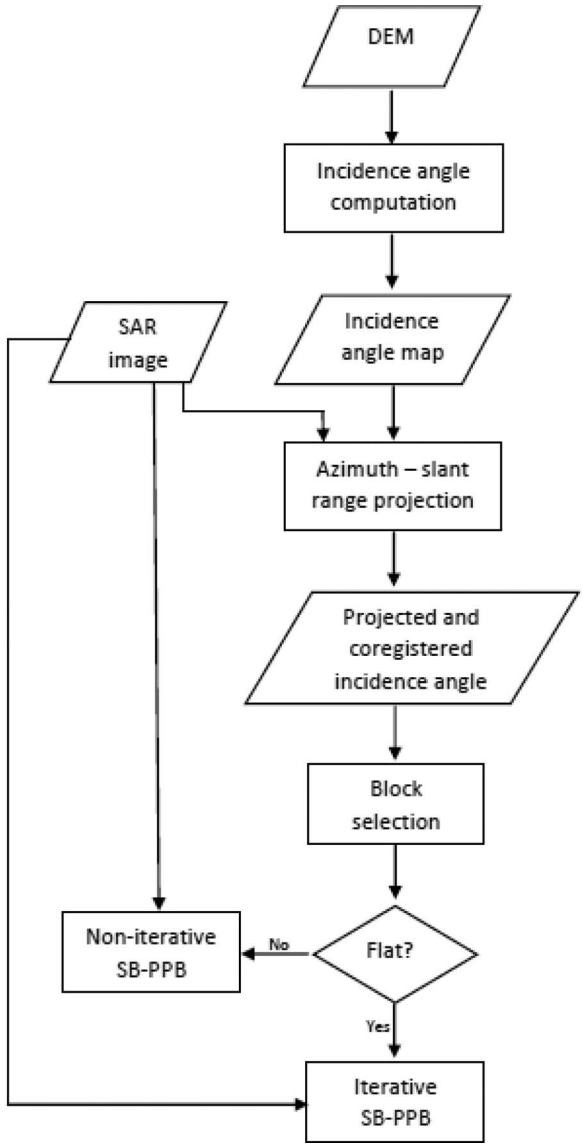

Fig. 1. Flowchart of the proposed SB-PPB filter. Iterations are adaptively performed only on flat areas, identified through a binary classification method based on the local incidence angle map.

V. Experimental Results

Performance evaluation of SAR despeckling techniques is not an easy task due to the absence of speckle-free SAR images to be used as reference. For this reason, numerous no-reference measures have been introduced to objectively evaluate the quality and accuracy of despeckling algorithms without resorting to reference images. However, on one hand, these measures do not provide a complete understanding of the algorithm behavior, and on the other hand, actual SAR images are not useful to analyze algorithm performances in some meaningful canonical situations. In order to provide a complete qualitative and quantitative analysis of the proposed filter performances and despeckling capabilities, the proposed filter is applied to both simulated and actual SAR images, and most of the performance measures introduced in [33] are used. In particular, the following performance parameters are evaluated: mean of image (MoI), variance of ratio (VoR), signal-to-noise ratio (SNR), mean structural similarity index measure (MSSIM), coefficient of variation (C_x), edge smearing (ES), and equivalent number of looks (ENL); refer to [33] and [52] for the definition and detailed description of these performance parameters. Since

TABLE I
PERFORMANCE PARAMETERS FOR THE SINUSOIDAL DEM

	MoI	VoR	SNR	ENL	MSSIM
Clean	1.000	1.000	∞	∞	1.000
Noisy	0.999	-	-3.455	1.03	0.963
SB-PPB (Proposed)	**0.997**	0.824	**17.451**	194.62	**1.000**
PPB non-it.	**0.997**	0.822	17.407	192.61	**1.000**
PPB 4-it.	**0.997**	0.822	17.171	187.66	**1.000**
SAR-BM3D	0.986	**0.865**	17.111	**440.94**	0.999

TABLE II
PERFORMANCE PARAMETERS FOR THE FRACTAL DEM

	MoI	VoR	SNR	C_x	MSSIM
Clean	1.000	1.000	∞	1.678	1.000
Noisy	0.989	-	0.225	2.576	0.963
SB-PPB (Proposed)	**0.951**	0.729	**5.837**	1.585	**0.990**
PPB non-it.	0.924	1.333	2.458	0.899	0.975
PPB 4-it.	0.942	**1.056**	4.578	1.469	0.983
SAR-BM3D	0.950	0.559	5.302	**1.661**	0.989

TABLE III
PERFORMANCE PARAMETERS FOR THE MIXED CASE

	MoI	VoR	SNR	C_x	ES	MSSIM	ENL
Clean	1.000	1.000	∞	1.833	0.000	1.000	∞
Noisy	0.998	-	-1.615	2.778	0.025	0.959	1.01
Adaptive SB-PPB	**0.987**	0.780	**11.165**	1.719	0.101	**0.997**	250.41
Non-iterative SB-PPB	0.986	0.785	11.130	1.717	0.288	**0.997**	253.43
4-iterative SB-PPB	**0.987**	0.871	10.320	**1.846**	0.112	0.996	244.43
PPB non-it.	0.976	1.114	8.540	0.858	0.289	0.993	251.47
PPB 4-it.	0.985	**0.945**	10.218	1.568	0.092	0.996	248.22
SAR-BM3D	0.971	0.725	10.878	1.777	**0.060**	**0.997**	**716.91**

TABLE IV
PERFORMANCE PARAMETERS FOR THE ACTUAL CASE

	MoI	VoR	C_x	ENL
Clean	1.000	1.000	1.188	∞
Noisy	1.000	-	1.955	0.83
SB-PPB (Proposed)	**0.986**	0.820	1.214	106.31
PPB non-it.	0.974	1.042	0.921	**110.94**
PPB 4-it.	0.984	**0.999**	1.074	107.20
SAR-BM3D	0.969	0.625	**1.199**	56.40

each parameter is intended to evaluate performance w.r.t. specific aspects of the algorithm or of the scene, in each experiment, a subset of the aforementioned parameters is used, as explicitly indicated both in the text and in the tables. For simulation purposes, we make use of SARAS, a SAR raw signal and image simulator [53]. Consistently with the proposed theoretical approach, the backscattered signal has been simulated using the SPM option of SARAS; furthermore, typical parameters of the Cosmo-SkyMed sensor have been set [54]. The speckle-free reference SAR images have been obtained through an average of 512 single-look realizations. On all noisy SAR images, the proposed adaptive SB-PPB filter is applied and compared to the SAR-BM3D, noniterative PPB, and PPB with four iterations. Default filter parameters defined in [25] and [23] are used for the PPB and SAR-BM3D, respectively. For the proposed filter, we use the same values of the parameters used for the PPB, apart from the T_{fil} parameter that, only in the first iteration, assumes different values in order to take into account the different kind of *a priori* information. In this case, best results are obtained, setting it equal to 1.3. Whenever iterations are performed, the default PPB value for T_{fil} is used. The binary classification is performed, subdividing the image in distinct blocks of size 256×256 and evaluating the standard deviation of the local incidence angle map: a region is classified as flat if the standard deviation of the incidence angle is sufficiently low. We empirically set a threshold of 2°. Furthermore, a search window size of 21×21 and a patch size of 7×7 are used both for the proposed and PPB filters, while a search window size of 39×39 is used for the SAR-BM3D filter. It is noteworthy that the proposed approach provides a direct improvement of the PPB filter, to which the proposed SB-PPB should be primarily compared. The best performances for each case and for each parameter are highlighted in boldface in Tables I–IV for the sake of clarity.

A. Results on Simulated SAR Images

This section presents numerical and visual results regarding the application of the proposed despeckling algorithm on three 512×512 Cosmo/SkyMed SAR images simulated using SARAS. In particular, the SAR images are simulated in the presence of a synthesized sinusoidal (Fig. 2) and fBm (Fig. 3) DEM, with microscopic roughness fractal parameters $H = 0.8$ and $T = 10^{-4}$ m, relative dielectric constant $\varepsilon_r = 4$, and conductivity $\sigma_c = 10^{-2}$ S/m. The fBm DEM presents the same fractal parameter values also at macroscopic scales. In order to test the effectiveness of the adaptive procedure, the proposed algorithm is applied also to a more realistic scenario in which both topographic- and nontopographic-induced SAR intensity variations are present (Fig. 4). In this experiment, the adaptive scheme is compared also to the noniterative and (nonadaptive) purely iterative versions of the proposed algorithm. Performance evaluation is carried out by computing the proper metrics in each case. In particular, MoI, VoR, SNR, and MSSIM are evaluated in all cases; in the sinusoidal case, the ENL is also computed, while in the fractal case, the coefficient of variation C_x is computed to evaluate the textural preservation capability of the despeckling filters. In the mixed case, ENL, ES, and C_x are all properly evaluated. Single-look SAR images are shown in Figs. 2(a), 3(a), and 4(a), respectively, while the reference 512-look images are depicted in Figs. 2(b), 3(b), and 4(b).

Concerning the sinusoidal case, the proposed SB-PPB technique [Fig. 2(c)], together with the PPB filter [Fig. 2(e)–(f)], provides the best results, both visually and quantitatively (as Table I shows), in preserving the continuous spatial variation of the SAR image intensity. SAR-BM3D [Fig. 2(d)] provides the worst results in this case, both visually and quantitatively, introducing visible artifacts in the despeckled image. The good performance of SAR-BM3D in terms of ENL is also partly due to the presence of oversmoothed block-like artifacts in the area used to evaluate the ENL [see Fig. 2(a)]. The slow-varying topography justifies the similarity in the performances of the proposed technique and the PPB filter (see Table I), while the absence of rapid variations in the image ensures an extremely fast convergence of PPB, i.e., iterations do not provide a significant improvement w.r.t. the noniterative PPB.

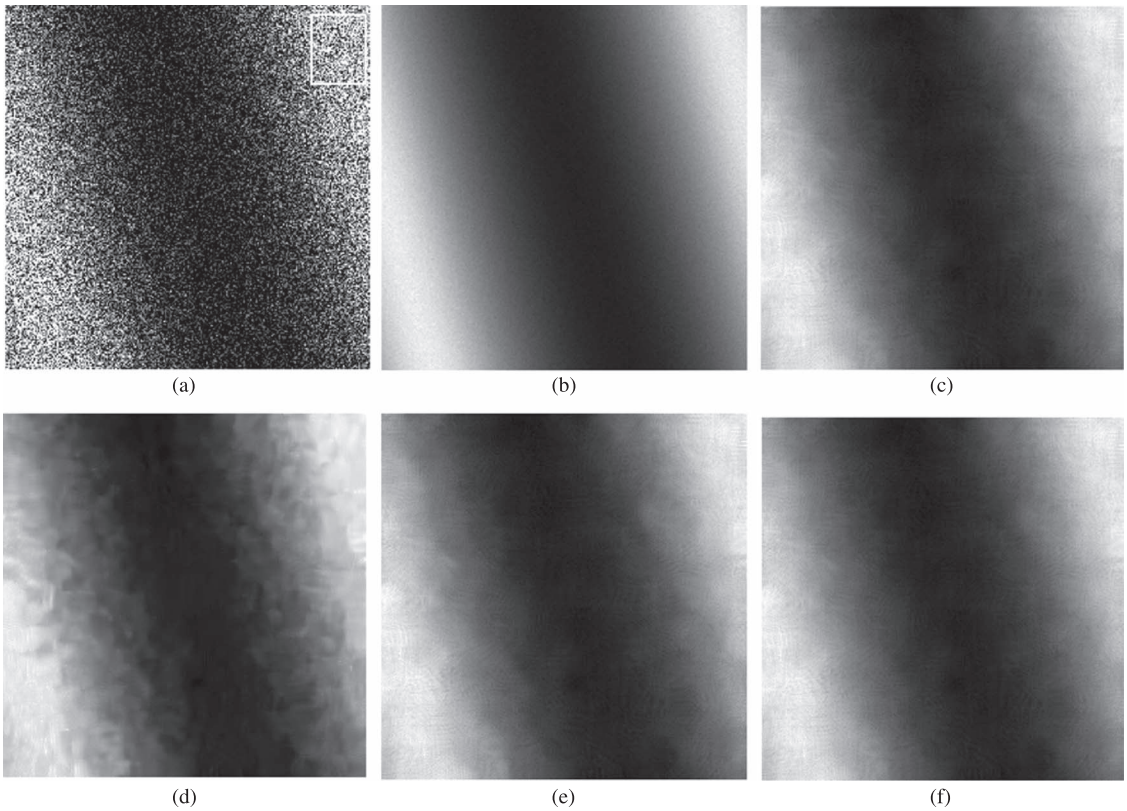

Fig. 2. (a) 512 × 512 simulated single-look SAR image in the presence of a sinusoidal topography, microscopic roughness of fractal parameters $H = 0.8$ and $T = 10^{-4}$ m, and electromagnetic parameters $\varepsilon_r = 4$ and $\sigma_c = 10^{-2}$ S/m, with indication of the area selected for the average ENL evaluation (white box). (b) 512-look reference image. (c) SB-PPB. (d) SAR-BM3D. (e) Four-iterative PPB. (f) Noniterative PPB.

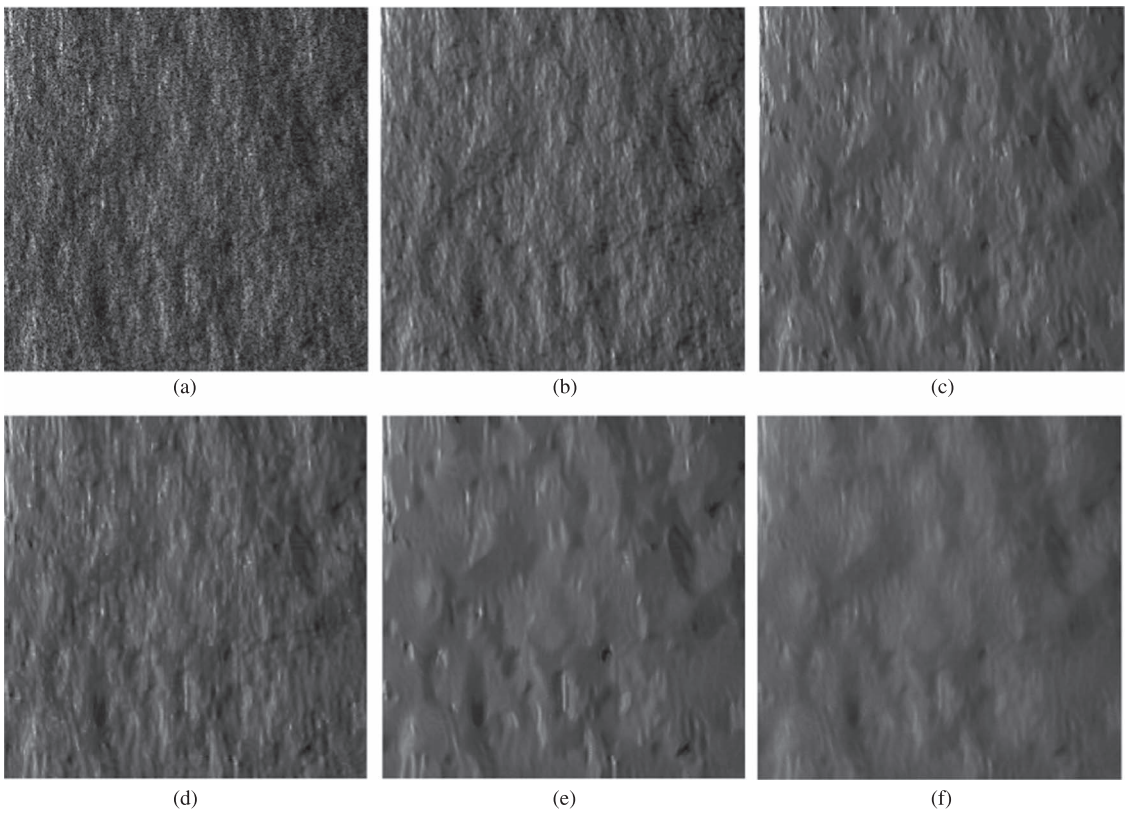

Fig. 3. (a) 512 × 512 simulated single-look SAR image in the presence of an fBm topography of fractal parameters $H = 0.8$ and $T = 10^{-4}$ m, and electromagnetic parameters $\varepsilon_r = 4$ and $\sigma_c = 10^{-2}$ S/m. (b) 512-look reference image. (c) SB-PPB. (d) SAR-BM3D. (e) Four-iterative PPB. (f) Noniterative PPB.

Turning to the fractal case [Fig. 3(a)], the knowledge of the underlying topography is responsible for a huge improvement of the despeckling capability of the PPB filter, as Fig. 3(c) and (f) shows, also considering its iterative version [Fig. 3(e)]. As shown in Table II, in this case, owing to the *a priori* knowledge of the local incidence angle map, the proposed approach provides the best results, also w.r.t. SAR-BM3D, particularly in terms of SNR. It provides also a preservation of the textural content of the sensed scene that is better with respect to the noniterative PPB and comparable to the SAR-BM3D, as demonstrated by the coefficient of variation and the structural similarity index.

In the previous two examples, due to the presence of a significant topography, the adaptive algorithm does not require to perform iterations. Fig. 4(a) and (b) shows the single-look and 512-look SAR images, respectively, in the case of a "mixed" scenario. The left part of the image consists of a flat region with four squares presenting different electromagnetic parameters: in particular, the brightest square simulates damp soil ($\varepsilon_r = 10,\ \sigma_c = 10^{-2}$ S/m), the middle gray-level squares simulate dry soil ($\varepsilon_r = 4,\ \sigma_c = 10^{-3}$ S/m), and the darkest one simulates the sea ($\varepsilon_r = 80,\ \sigma_c = 4$ S/m). The right part is the SAR image of a 2-D fBm surface with the same parameters used in the previous experiment. The local incidence angle map is depicted in Fig. 4(i). Fig. 4(g) shows the outcome of the noniterative version of the proposed despeckling algorithm, i.e., no iterations are applied to the entire image. The noniterative scheme provides a good speckle reduction on the overall image with a satisfactory detail preservation in the nonflat part of the image (see also the coefficient of variation and the SNR in Table III). However, in the left part, where nontopographic-induced intensity variations are present, the lack of *a priori* knowledge about electromagnetic parameter variations makes the edges in the left part to be largely smoothed: in this case, iterations are needed to enhance edge preservation capability. Performing iterations over the entire image improves edge preservation capability of the filter, at the cost of a much greater execution time, since iterations are performed also in nonflat regions, in which they are theoretically useless and also detrimental for detail preservation, as Fig. 4(h) shows. To this aim, the proposed adaptive scheme introduces iterations in a smart and adaptive way only in those regions where nontopographic-related intensity variations are present. In this case, the adaptive scheme performs iterations only in the left part of the image [Fig. 4(c)], thus greatly reducing the execution time w.r.t. the pure iterative scheme, in which iterations are performed on the whole image [Fig. 4(h)] and ensuring the same detail preservation provided by the noniterative scheme. A visual inspection of the results shows that the adaptive scheme provides better results w.r.t. both the noniterative and purely iterative versions of the proposed algorithm, maintaining the advantages of both schemes, namely, a good preservation of both textural details and edges. The proposed adaptive SB-PPB presents the best SNR, and in general, its performances are comparable to the SAR-BM3D, outperforming both the noniterative and iterative PPBs. This behavior is quantitatively confirmed by the performance parameters reported in Table III. In particular, the adaptive SB-PPB ensures the same detail preservation as the noniterative SB-PPB in the nonflat region (see the C_x parameter) and a comparable edge preservation as the iterative SB-PPB in the flat one (see the ES parameter).

B. Robustness of the Method With Respect to Scattering Model Inaccuracy

In this section, we test the robustness of the proposed despeckling algorithm with respect to inaccuracies of the employed scattering model. To this aim, we apply the proposed algorithm to a single-look SAR image simulated using a scattering model different from the SPM one of (8). In particular, we simulate a SAR image of a fractal DEM with $H = 0.8$ and $T = 10^{-4}$ m using an empirical scattering model according to which $\hat{\sigma} = \cos^4\theta$. However, in the algorithm, the fractal SPM scattering model was used as described in Section III. Performance is quantitatively evaluated via the MSE. The output of the algorithm is compared with the PPB and the SAR-BM3D filters in Fig. 5. In particular, Fig. 5(a) shows the 512×512 simulated single-look SAR image; the 512-look SAR image used as reference is depicted in Fig. 5(b). The output of the proposed algorithm is shown in Fig. 5(c), while Fig. 5(d)–(f) shows the filtered image using the SAR-BM3D and the original PPB with no iterations and four iterations, respectively. The lower dynamic of SAR data in the $\cos^4\theta$ case, due to the flatter scattering model, causes an evident oversmoothing in the PPB filter, in which iterations are not able to recover more details. The SB-PPB performs better than PPB both visually and quantitatively. Owing to the scattering distance term, a better detail preservation is reached, also in the presence of a different scattering behavior of the surface. The slightly better quantitative performance provided by SAR-BM3D is accompanied by a more visible blocky effect that could affect in some way the interpretation of the despeckled image.

We also test the robustness of the algorithm with respect to inaccuracy in the estimation of the Hurst coefficient. In particular, we apply the SB-PPB filter to the single-look SAR image in Fig. 3(a) simulated considering an fBm surface of fractal parameters $H = 0.8$ and $T = 10^{-4}$ m and the SPM scattering model as described in Section III. In order to simulate an error in the H estimation, in the filter, we assume $H = 0.6$ (a relative error of 25%). It turns out that the significant error on the H parameter causes a negligible performance degradation of about 3% (computed on the SNR), owing to the scattering model weaker dependence on H than on the incidence angle. Consequently, in the case of strict time requirements, it is possible to avoid the H estimation step, using a default value, e.g., $H = 0.8$, without a significative degradation of the performance.

C. Results on Actual SAR Image

The proposed algorithm is also applied to a 2700×2700 subset of an actual single-look stripmap Cosmo/SkyMed SAR image acquired over the Vesuvius-Mt. Somma complex close to Naples, Italy, on August 1, 2011. The image is relevant to an area almost free of man-made objects [Fig. 6(a)]. The radar look angle is 35°, the azimuth and slant range resolutions are

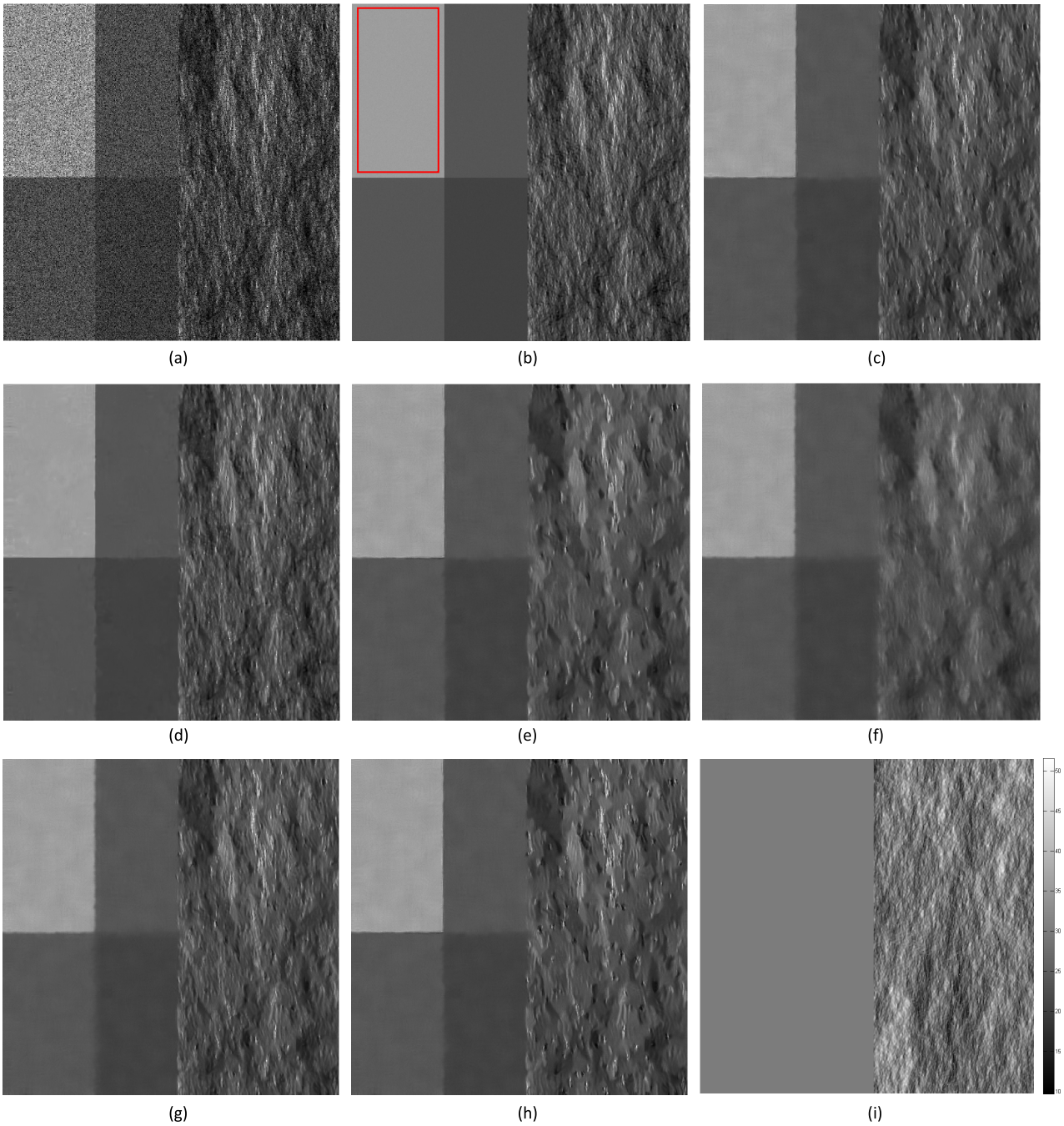

Fig. 4. (a) 512 × 512 simulated single-look SAR image in the presence of an fBm topography of fractal parameters $H = 0.8$ and $T = 10^{-4}$ m, and electromagnetic parameters $\varepsilon_r = 4$ and $\sigma_c = 10^{-2}$ S/m (right) and patches of different electromagnetic parameters—in particular, the brightest square simulates damp soil ($\varepsilon_r = 10,\ \sigma_c = 10^{-2}$ S/m), the middle gray-level squares simulate dry soil ($\varepsilon_r = 4,\ \sigma_c = 10^{-3}$ S/m), and the darkest one simulates sea ($\varepsilon_r = 80,\ \sigma_c = 4$ S/m). (b) 512-look reference image. The red box indicates the region in which the ENL is computed; the ES parameter is computed on the edge between the upper left and lower left squares. (c) Adaptive SB-PPB. (d) SAR-BM3D. (e) Four-iterative PPB. (f) Noniterative PPB. (g) Noniterative SB-PPB. (h) Four-iterative SB-PPB. (i) Local incidence angle map.

both equal to 2.5 m, while the pixel spacing values are 2.07 and 2.06 m in azimuth and ground range, respectively; the operating frequency is 9.6 GHz. The local incidence angle map [Fig. 6(b)] is obtained from a DEM acquired with a lidar system. Fig. 6(c) shows the proposed SB-PPB filter, Fig. 6(d) shows the SAR-BM3D, while Fig. 6(e) and (f) shows the four-iterative and noniterative PPB outcomes, respectively. The Hurst exponent has been evaluated through the algorithm proposed by Di Martino *et al.* in [28]. In this case, due to the absence of a reference image, performance is evaluated, computing all of the no-reference parameters, i.e., the MoI, VoR, C_x, and ENL. In order to evaluate the speckle reduction in homogeneous regions, we compute the average ENL in a region of homogeneous local incidence angle [white box in Fig. 6(a)]. Similarly, the coefficient of variation is computed on a homogeneously textured region of the Mt. Somma [black box in Fig. 6(a)]. The proposed scattering-based technique exhibits better performance than the PPB for what concerns the textural information preservation,

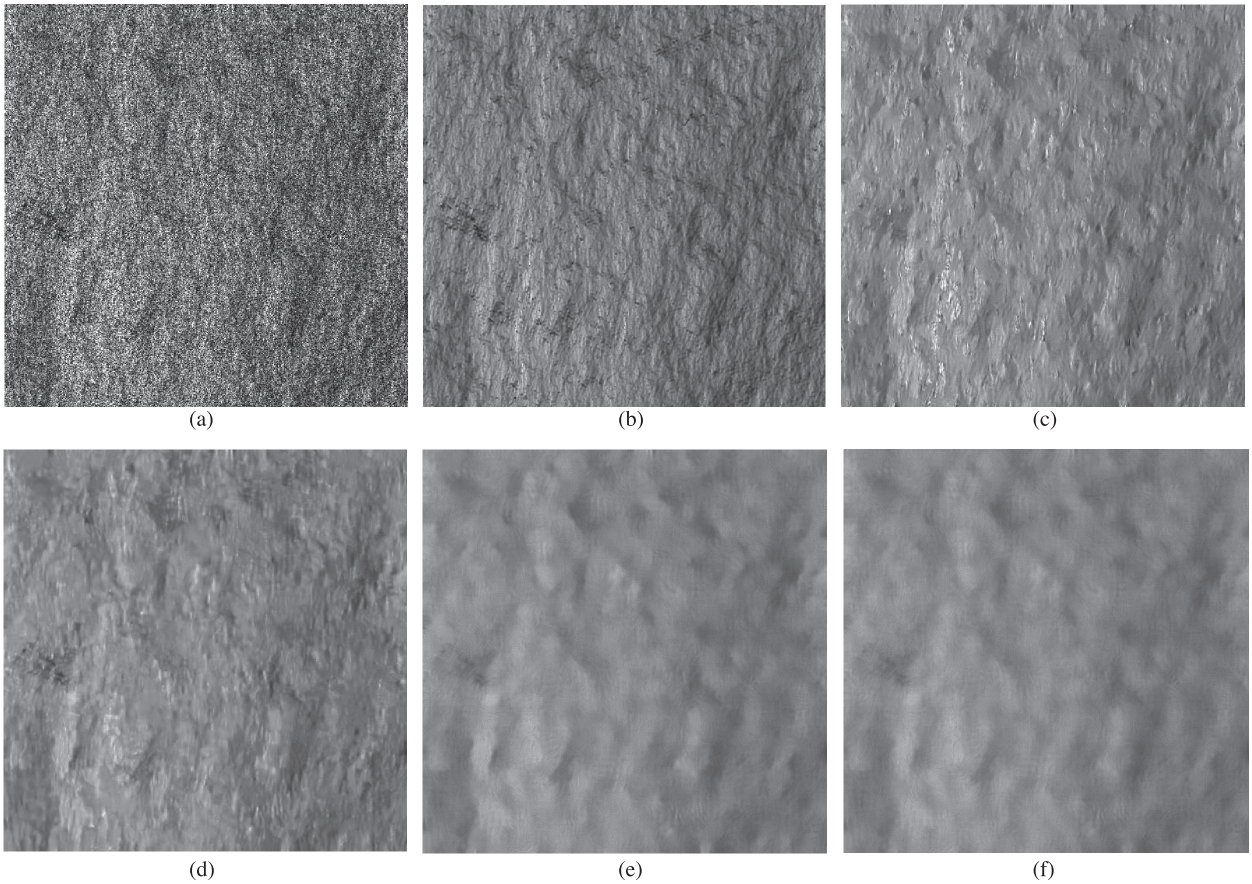

Fig. 5. (a) Single-look SAR image of a fractal DEM with $H = 0.8$ and $T = 10^{-4}$ m simulated via the $\cos^4\theta$ scattering model. (b) 512-look SAR image used as reference and simulated via the $\cos^4\theta$ scattering model. (c) SB-PPB filter. MSE $= 0.153$. (d) SAR-BM3D. MSE $= 0.150$. (e) PPB with four iterations. MSE $= 0.187$. (f) Noniterative PPB. MSE $= 0.188$. For MSE evaluation, the single-look and reference SAR images are normalized to the mean value of the reference SAR image. Owing to the scattering distance term, the SB-PPB filter performs better than the original PPB both visually and quantitatively also in the presence of a different scattering model.

as shown both in Table IV (see the C_x parameter) and in Figs. 6 and 7. Owing to the introduction of the scattering term, good enhancement and preservation of details are obtained, as shown in Fig. 6(c)–(f). With regard to speckle reduction in homogeneous areas, the proposed algorithm shows comparable performances w.r.t. PPB, as Fig. 6(c) and the ENL show. In conclusion, in this case, no algorithm is the best for all metrics, PPB exhibits a better speckle reduction, while SAR-BM3D and the proposed filter show a better detail preservation (see the zoomed region in Fig. 7). It can be reasonably argued that the difficulty to correctly evaluate performance with actual SAR images makes visual inspection the best tool for performance evaluation. A simple visual inspection suggests that the SB-PPB filter, owing to the introduction of *a priori* knowledge about the scattering behavior of the scene, ensures a better detail preservation w.r.t. the PPB filter and exhibits an overall performance comparable to the SAR-BM3D.

Finally, a last remark about computational time is in order. All of the experiments were carried out on a dual-core, 3-GHz clock, and 8-GB RAM PC. Application of the proposed adaptive SB-PPB algorithm (including H estimation and coregistration steps) to the actual 2700×2700 pixel SAR image of Fig. 6 required about 11 min, of which one and a half for the coregistration step and 3 for the H estimation step (the latter, however, can be avoided without significant performance degradation, thus reducing the total processing time to 8 min). Conversely, PPB required about 6 and about 25 min in its noniterative and iterative versions, respectively. Finally, SAR-BM3D required about 1 h. Accordingly, it is confirmed that the proposed adaptive SB-PPB algorithm, complete of azimuth–slant range projection and H estimation steps, exhibits an execution time on the same order of the one of PPB; conversely, the SAR-BM3D filter is more computationally demanding due to the higher computational complexity of the approach and the larger default search window.

VI. Conclusion

In this paper, the novel concept of taking into account the scattering mechanisms within the despeckling problem has been presented and implemented via an NLM approach, providing an improvement of the PPB filter—the SB-PPB filter—through a proper insertion of *a priori* information about the scattering from the resolution cell. In particular, starting from the PPB filter proposed in [25], we have derived a new patch similarity measure introducing a fractal scattering model suitable for natural surfaces for the weight definition. Due to the strong dependence of the scattered field on the local incidence

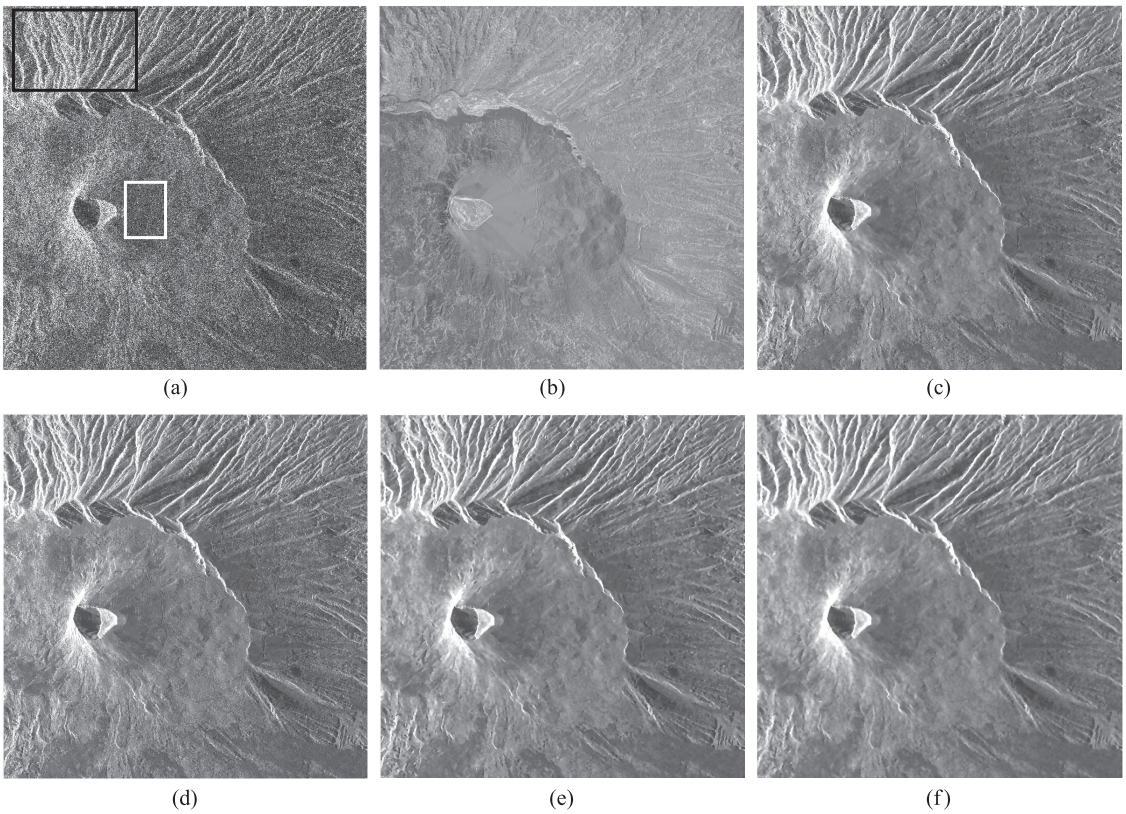

Fig. 6. (a) 2700 × 2700 subset of a Cosmo/SkyMed single-look stripmap SAR image with indication of the areas selected for coefficient of variation (black box) and average ENL (white box) computation. (b) Local incidence angle in azimuth–slant range derived from a DEM obtained with a lidar system and used as *a priori* knowledge in the SB-PPB filter. (c) Adaptive SB-PPB. (d) SAR-BM3D. (e) Four-iterative PPB. (f) Noniterative PPB.

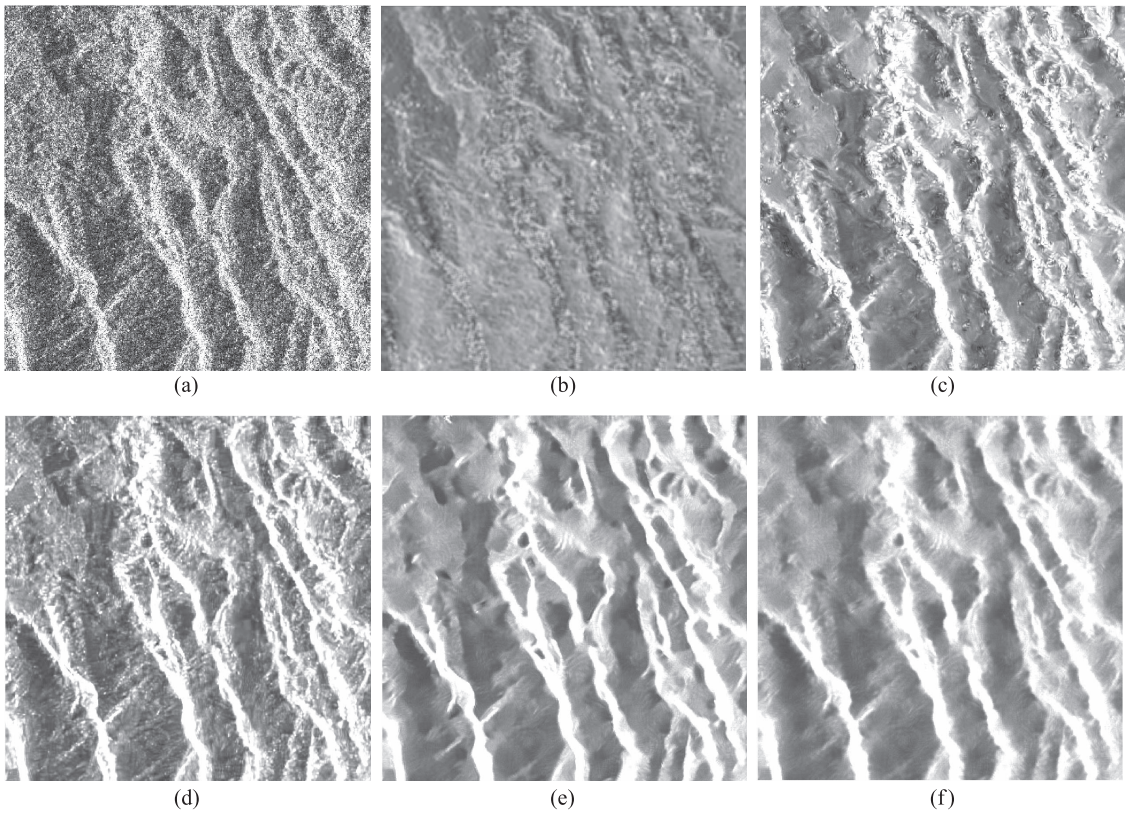

Fig. 7. Zoom of a portion of the black-marked region of Fig. 6. (a) Single-look image. (b) Local incidence angle in azimuth–slant range. (c) Adaptive SB-PPB. (d) SAR-BM3D. (e) Four-iterative PPB. (f) Noniterative PPB. Oversmoothing of the PPB filter is clearly visible. SAR-BM3D and SB-PPB succeed better in preserving texture and details.

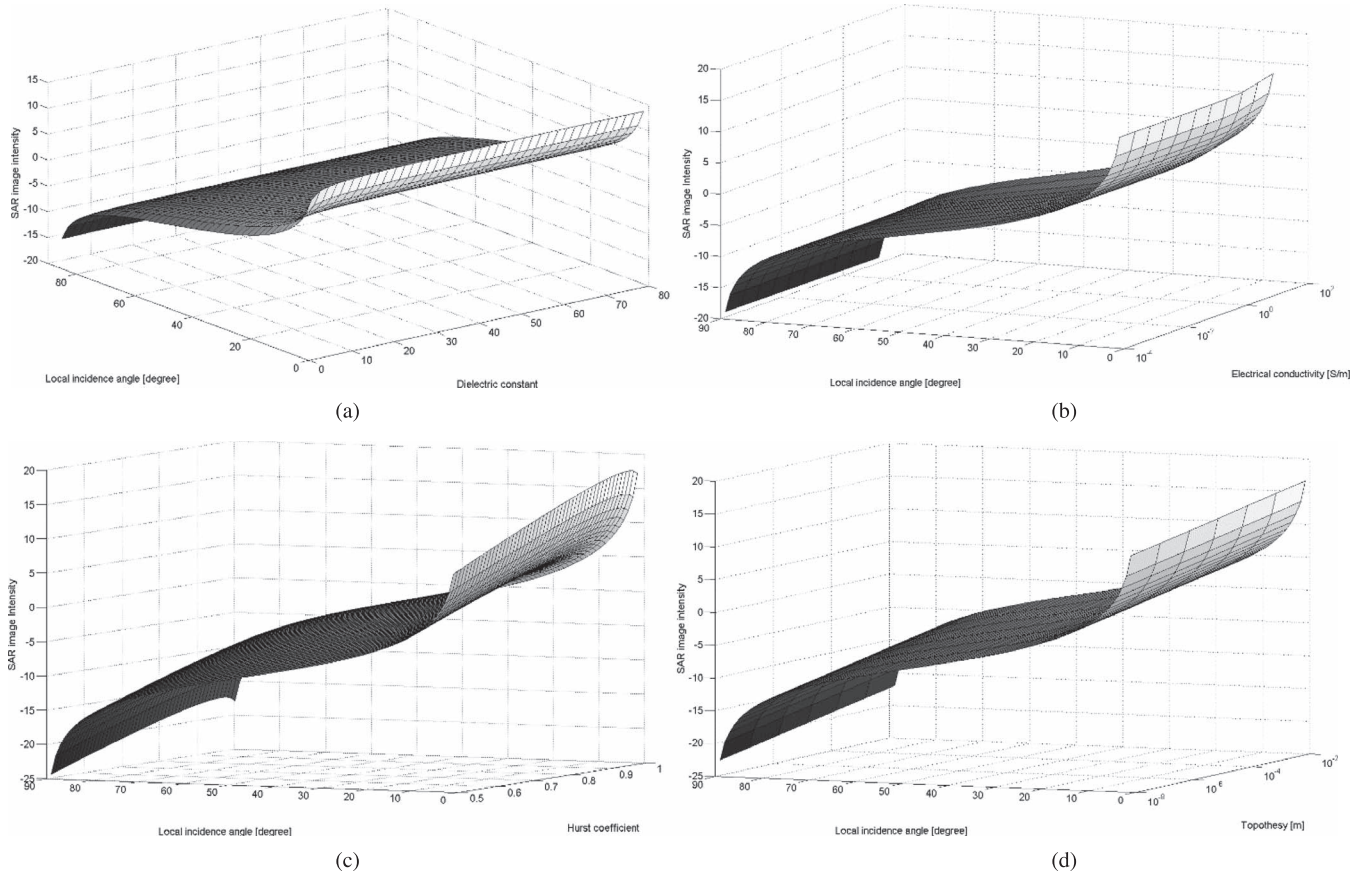

Fig. 8. NRCS dependence [see (8)]. (a) Incidence angle versus dielectric constant assuming $T = 10^{-4}$ m, $H = 0.8$, and $\sigma = 10^{-2}$ S/m. (b) Incidence angle versus electrical conductivity assuming $T = 10^{-4}$ m, $H = 0.8$, and $\varepsilon_r = 10$. (c) Incidence angle versus Hurst coefficient assuming $T = 10^{-4}$ m, $\varepsilon_r = 10$, and $\sigma = 10^{-2}$ S/m. (d) Incidence angle versus topothesy assuming $\varepsilon_r = 10$, $H = 0.8$, and $\sigma = 10^{-2}$ S/m. All graphs are in logarithmic scale on the z-axis; electrical conductivity and topothesy axes are in log scale, too.

angle, the proposed distance reduces to a proper nonlinear distance in incidence angle. Owing to the scattering distance term, we have shown that the SB-PPB performs better than the original PPB filter, even in cases in which scattering from the surface is not accurately described by the fractal scattering model employed in this paper.

The proposed technique requires an *a priori* knowledge of the underlying topography, i.e., a DEM in the azimuth–slant range geometry of the SAR sensor coregistered with the noisy SAR image is required. The Hurst exponent describing the soil roughness can be easily estimated through the approach proposed in [28]. However, we have shown that the proposed filter is quite robust against errors on the H coefficient, so that, if time requirements are very strict, it is possible to use a typical value for H without a significative performance degradation. The proposed filter is originally designed for nonflat natural surfaces, i.e., for SAR images in which the intensity variations are mostly due to the topography. However, in order to deal also with flat regions and nontopographic-induced backscattering variations, we have proposed an iterative scheme that, in a smart and adaptive way, performs iterations only in flat regions in which the noniterative procedure does not provide a good reliability in terms of edge preservation if compared to the state of the art. To this aim, we have proposed a simple flat–nonflat binary classification method in order to discriminate topographic-related from nontopographic-related SAR intensity variations. The proposed binary classification technique is based on the DEM, and therefore, it does not require additional information. The adaptive scheme extends the applicability of the filter to different scenarios in which the single-bounce scattering is not the dominant scattering phenomenon, such as vegetated areas or suburban areas.

In order to evaluate the effectiveness of the filter and its capability of speckle reduction, an extensive experimental part has been set up, using both simulated and actual SAR images. The proposed SB-PPB filter exhibits objective performances comparable or superior to competing techniques on simulated single-look SAR images and satisfactory subjective quality on the actual SAR image considered. It is also noteworthy that the proposed algorithm "converges" to the iterative PPB in the presence of totally flat topography. The proposed adaptive SB-PPB filter provides promising results especially in those cases in which topography is the main source of SAR intensity variations. With SAR images of nonflat surfaces, the proposed algorithm outperforms both the noniterative and iterative PPB filters, both in terms of speckle reduction and detail preservation, owing to the *a priori* topographic knowledge.

The authors are currently studying the possibility to estimate the local incidence angle map, needed by the filter, from a single SAR image. Such a retrieval procedure would be useful in the proposed despeckling approach since the *a priori* knowledge could be estimated from the image itself without requiring extra information, but it would be also relevant per se since it

could be useful in a number of applications. In addition, the proposed scattering-based approach can be easily applied to other despeckling filters, such as SAR-BM3D. This possibility is currently under investigation by the authors. Last but not least, an approach similar to the one presented here for the scene topography may be used to take into account some additional *a priori* information about the sensed scene, in order to move a step further toward a more meaningful physical-based and object-oriented despeckling approach.

APPENDIX
SENSITIVITY ANALYSIS OF THE DIRECT MODEL

The direct model presented in Section III [see (8)] identifies the numerous parameters (relevant to both the sensor and the surface) on which SAR imagery depends, namely, the dielectric constant, electrical conductivity, and microscopic and macroscopic roughness. The use of analytical models for both scattering phenomena and surface shape makes us more aware on how these parameters affect SAR image formation. At the same time, a proper modeling of the problem provides the possibility to estimate the parameters of interest. Fig. 8 shows the dependence of the intensity SAR image, evaluated through (8), against the local incidence angle, the dielectric constant, the Hurst coefficient, and the topothesy. All of the graphs show that the major contribution to SAR image formation is due to the topography, i.e., to the local incidence angle. In particular, it is important to note that also the microscopic roughness, i.e., Hurst coefficient and topothesy, has a minor influence on SAR image intensity with respect to the macroscopic one.

REFERENCES

[1] C. Oliver and S. Quegan, *Understanding Synthetic Aperture Radar Images*. Raleigh, NC, USA: SciTech, 2004.

[2] R. Touzi, "A review of speckle filtering in the context of estimation theory," *IEEE Trans. Geosci. Remote Sens.*, vol. 40, no. 11, pp. 2392–2404, Nov. 2002.

[3] F. Argenti, A. Lapini, T. Bianchi, and L. Alparone, "A tutorial on speckle reduction in synthetic aperture radar images," *IEEE Geosci. Remote Sens. Mag.*, vol. 1, no. 3, pp. 6–35, Sep. 2013.

[4] C.-A. Deledalle, L. Denis, G. Poggi, F. Tupin, and L. Verdoliva, "Exploiting patch similarity for SAR image processing: The nonlocal paradigm," *IEEE Signal Process. Mag.*, vol. 31, no. 4, pp. 69–78, Jul. 2014.

[5] M. Levesque and H. Arsenault, "Combined homomorphic and local-statistics processing for restoration of images degraded by signal-dependent noise," *Appl. Opt.*, vol. 23, no. 6, pp. 845–850, Mar. 1984.

[6] P. F. Yan and C. H. Chen, "An algorithm for filtering multiplicative noise in wide range," *Traitement du Signal*, vol. 3, no. 2, pp. 91–96, 1986.

[7] S. Solbo and T. Eltoft, "Homomorphic wavelet-based statistical despeckling of SAR images," *IEEE Trans. Geosci. Remote Sens.*, vol. 42, no. 4, pp. 711–721, Apr. 2004.

[8] S. Chitroub, A. Houacine, and B. Sansal, "Statistical characterisation and modelling of SAR images," *Signal Process.*, vol. 82, no. 1, pp. 69–92, 2002.

[9] A. Frery, H.-J. Muller, C. Yanasse, and S. Sant'Anna, "A model for extremely heterogeneous clutter," *IEEE Trans. Geosci. Remote Sens.*, vol. 35, no. 3, pp. 648–659, May 1997.

[10] J. Goodman, "Some fundamental properties of speckle," *J. Opt. Soc. Amer.*, vol. 66, no. 11, pp. 1145–1150, 1976.

[11] Y. Yu and S. T. Acton, "Speckle reducing anisotropic diffusion," *IEEE Trans. Image Process.*, vol. 11, no. 11, pp. 1260–1270, Nov. 2002.

[12] J. S. Lee, "Digital image enhancement and noise filtering by use of local statistics," *IEEE Trans. Pattern Anal. Mach. Intell.*, vol. PAMI-2, no. 2, pp. 165–168, Mar. 1980.

[13] J. S. Lee, "Refined filtering of image noise using local statistics," *Comput. Graph. Image Process.*, vol. 15, no. 4, pp. 380–389, Apr. 1981.

[14] V. S. Frost, J. A. Stiles, K. S. Shanmugan, and J. C. Holtzman, "A model for radar images and its application to adaptive digital filtering of multiplicative noise," *IEEE Trans. Pattern Anal. Mach. Intell.*, vol. PAMI-4, no. 2, pp. 157–166, Mar. 1982.

[15] D. T. Kuan, A. A. Sawchuk, T. C. Strand, and P. Chavel, "Adaptive noise smoothing filter for images with signal-dependent noise," *IEEE Trans. Pattern Anal. Mach. Intell.*, vol. PAMI-7, no. 2, pp. 165–177, Mar. 1985.

[16] R. Touzi, A. Lopes, and P. Bousquet, "A statistical and geometrical edge detector for SAR images," *IEEE Trans. Geosci. Remote Sens.*, vol. 26, no. 6, pp. 764–773, Nov. 1988.

[17] A. Lopes, R. Touzi, and E. Nezry, "Adaptive speckle filters and scene heterogeneity," *IEEE Trans. Geosci. Remote Sens.*, vol. 28, no. 6, pp. 992–1000, Nov. 1990.

[18] M. Hebar, D. Gleich, and Z. Cucej, "Autobinomial model for SAR image despeckling and information extraction," *IEEE Trans. Geosci. Remote Sens.*, vol. 47, no. 8, pp. 2818–2835, May 2009.

[19] A. Lopes, E. Nezry, R. Touzi, and H. Laur, "Maximum *a posteriori* speckle filtering and first order texture models in SAR images," in *Proc. IEEE Int. Geosci. Remote Sens. Symp.*, May 1990, vol. 3, pp. 2409–2412.

[20] F. Argenti, T. Bianchi, and L. Alparone, "Multiresolution MAP despeckling of SAR images based on locally adaptive generalized Gaussian pdf modeling," *IEEE Trans. Image Process.*, vol. 15, no. 11, pp. 3385–3399, Nov. 2006.

[21] T. Bianchi, F. Argenti, and L. Alparone, "Segmentation-based MAP despeckling of SAR images in the undecimated wavelet domain," *IEEE Trans. Geosci. Remote Sens.*, vol. 46, no. 9, pp. 2728–2742, Sep. 2008.

[22] Q. Gao, Y. Zhao, and Y. Lu, "Despeckling SAR images using stationary wavelet transform combining with directional filter banks," *Appl. Math. Comput.*, vol. 205, no. 2, pp. 517–524, 2008.

[23] S. Parrilli, M. Poderico, C. V. Angelino, and L. Verdoliva, "A nonlocal SAR image denoising algorithm based on LLMMSE wavelet shrinkage," *IEEE Trans. Geosci. Remote Sens.*, vol. 50, no. 2, pp. 606–616, Feb. 2012.

[24] A. Buades, B. Coll, and J. M. Morel, "A review of image denoising algorithms, with a new one," *Multiscale Model. Simul.*, vol. 4, no. 2, pp. 490–530, 2005.

[25] C.-A. Deledalle, L. Denis, and F. Tupin, "Iterative weighted maximum likelihood denoising with probabilistic patch-based weights," *IEEE Trans. Image Process.*, vol. 18, no. 12, pp. 2661–2672, Dec. 2009.

[26] C.-A. Deledalle, L. Denis, F. Tupin, A. Reigber, and M. Jäger, "NL-SAR: A unified nonlocal framework for resolution-preserving (Pol)(In) SAR denoising," *IEEE Trans. Geosci. Remote Sens.*, vol. 53, no. 4, pp. 2021–2038, Apr. 2015.

[27] G. Franceschetti and R. Lanari, *Synthetic Aperture Radar (SAR) Processing*. New York, NY, USA: CRC Press, 1999.

[28] G. Di Martino, D. Riccio, and I. Zinno, "SAR imaging of fractal surfaces," *IEEE Trans. Geosci. Remote Sens.*, vol. 50, no. 2, pp. 630–644, Feb. 2012.

[29] G. Franceschetti and D. Riccio, *Scattering, Natural Surfaces and Fractals*. Burlington, MA, USA: Academic, 2007.

[30] P. Beckmann and A. Spizzichino, *The Scattering of Electromagnetic Waves From Rough Surfaces*. Norwood, MA, USA: Artech House, 1987.

[31] A. K. Fung, *Microwave Scattering and Emissions. Models and Their Applications*. Norwood, MA, USA: Artech House, 1994.

[32] G. Di Martino, A. Di Simone, A. Iodice, D. Riccio, and G. Ruello, "Non-local means SAR despeckling based on scattering," in *Proc. IEEE Int. Geosci. Remote Sens. Symp.*, Milan, Italy, Jul. 2015, pp. 3172–3174.

[33] G. Di Martino, M. Poderico, G. Poggi, D. Riccio, and L. Verdoliva, "Benchmarking framework for SAR despeckling," *IEEE Trans. Geosci. Remote Sens.*, vol. 52, no. 3, pp. 1596–1615, Mar. 2014.

[34] J.-S. Lee, "Digital image smoothing and the sigma filter," *Comput. Vis., Graph., Image Process.*, vol. 24, no. 2, pp. 255–269, 1983.

[35] J.-S. Lee, "A simple speckle smoothing algorithm for synthetic aperture radar images," *IEEE Trans. Syst., Man, Cybern.*, vol. SMC-13, no. 1, pp. 85–89, Jan. 1983.

[36] K. Dabov, A. Foi, V. Katkovnik, and K. Egiazarian, "Image denoising by sparse 3-D transform-domain collaborative filtering," *IEEE Trans. Image Process.*, vol. 16, no. 8, pp. 2080–2095, Aug. 2007.

[37] K. Falconer, *Fractal Geometry*. Chichester, U.K.: Wiley, 1990.

[38] J. S. Feder, *Fractals*. New York, NY, USA: Plenum, 1988.

[39] B. Mandelbrot, *The Fractal Geometry of Nature*. New York, NY, USA: Freeman, 1983.

[40] T. Austin, A. W. England, and G. H. Wakefield, "Special problems in the estimation of power-law spectra as applied to topographical modeling," *IEEE Trans. Geosci. Remote Sens.*, vol. 32, no. 4, pp. 928–939, Jul. 1994.

[41] S. R. Brown and C. H. Scholz, "Broad-band study of the topography of natural rock surfaces," *J. Geophys. Res.*, vol. 90, no. B14, pp. 12 575–12v582, Dec. 1985.
[42] G. Di Martino, A. Iodice, D. Riccio, and G. Ruello, "Equivalent number of scatterers for SAR speckle modeling," *IEEE Trans. Geosci. Remote Sens.*, vol. 52, no. 5, pp. 2555–2564, May 2014.
[43] W. Dierking, "Quantitative roughness characterization of geological surfaces and implications for radar signature analysis," *IEEE Trans. Geosci. Remote Sens.*, vol. 37, no. 5, pp. 2397–2412, Sep. 1999.
[44] G. Franceschetti, A. Iodice, M. Migliaccio, and D. Riccio, "Scattering from natural rough surfaces modeled through fractal Brownian motion two-dimensional processes," *IEEE Trans. Antennas Propag.*, vol. 47, no. 9, pp. 1405–1415, Sep. 1999.
[45] M. K. Shepard, B. A. Campbell, M. H. Bulmer, T. G. Farr, and L. R. Gaddis, "The roughness of natural terrain: A planetary and remote sensing perspective," *J. Geophys. Res.*, vol. 106, no. E12, pp. 32 777–32 795, Dec. 2001.
[46] G. Franceschetti, A. Iodice, S. Maddaluno, and D. Riccio, "A fractal-based theoretical framework for retrieval of surface parameters from electromagnetic backscattering data," *IEEE Trans. Geosci. Remote Sens.*, vol. 38, no. 2, pp. 641–650, Mar. 2000.
[47] G. Di Martino, A. Di Simone, A. Iodice, D. Riccio, and G. Ruello, "On shape from shading and SAR images: An overview and a new perspective," in *Proc. IEEE Int. Geosci. Remote Sens. Symp.*, 2014, pp. 1333–1336.
[48] A. Iodice, A. Natale, and D. Riccio, "Retrieval of soil surface parameters via a polarimetric two-scale model," *IEEE Trans. Geosci. Remote Sens.*, vol. 49, no. 7, pp. 2531–2547, Jul. 2011.
[49] T. G. Farr *et al.*, "The Shuttle Radar Topography Mission," *Rev. Geophys.*, vol. 45, May 2007, Art. no. RG2004.
[50] "Earth Explorer," U.S. Geol. Survey, Reston, VA, USA, [Accessed Feb. 11, 2015]. [Online]. Available: http://earthexplorer.usgs.gov/.
[51] U.S.I.T.C.- città metropolitana di Napoli, [Accessed Feb. 11, 2015]. [Online]. Available: http://sit.cittametropolitana.na.it/lidar.html.
[52] Z. Wang, A. C. Bovik, H. R. Sheikh, and E. P. Simoncelli, "Image quality assessment: From error visibility to structural similarity," *IEEE Trans. Image Process.*, vol. 13, no. 4, pp. 1–14, Apr. 2004.
[53] G. Franceschetti, M. Migliaccio, D. Riccio, and G. Schirinzi, "SARAS: A SAR raw signal simulator," *IEEE Trans. Geosci. Remote Sens.*, vol. 30, no. 1, pp. 110–123, Jan. 1992.
[54] "COSMO-SkyMed System Description & User Guide," Italian Space Agency (ASI), Rome, Italy. [Online]. Available: http://www.cosmo-skymed.it/docs/ASI-CSM-ENG-RS-093-A-CSKSysDescriptionAndUserGuide.pdf.

Gerardo Di Martino (S'06–M'09) was born in Naples, Italy, on June 22, 1979. He received the Laurea degree (*cum laude*) in telecommunication engineering and the Ph.D. degree in electronic and telecommunication engineering from the University Federico II, Naples, in 2005 and 2009, respectively.

From 2009 to 2010, he conducted research on indoor electromagnetic propagation and localization of unknown transmitters with the Department of Biomedical, Electronic and Telecommunication Engineering, University of Naples Federico II, through grants from the same university. From 2010 to 2012, he worked on a project financed by the Italian Space Agency aimed at the development of techniques for information extraction from high-resolution SAR images of urban and natural areas. From 2012 to 2014, he was a Research Fellow with the Department of Electrical Engineering and Information Technology, University of Naples Federico II, working on a project regarding maritime surveillance with SAR data. From 2014 to 2015, he conducted research in the field of electromagnetic propagation in harbor scenarios and innovative network architectures through grants received from the Italian National Consortium for Telecommunications. He is currently a Research Fellow with the Department of Electrical Engineering and Information Technology, University of Naples Federico II, working on a project regarding sparse antenna arrays. His main research interests include microwave remote sensing and electromagnetics, with particular focus on modeling of the electromagnetic scattering from natural surfaces and urban areas, SAR signal processing and simulation, information retrieval from SAR data, and remote sensing techniques for developing countries.

Alessio Di Simone was born in Torre del Greco, Naples, Italy, on September 11, 1989. He received the B.Sc. and M.Sc. Laurea degrees (*cum laude*) in telecommunication engineering in 2011 and 2013, respectively, from the University of Naples "Federico II," Naples, where he is currently working toward the Ph.D. degree in information technology and electrical engineering.

His main research interests are in the field of microwave remote sensing and electromagnetics: modeling of the electromagnetic scattering from natural surfaces, SAR data simulation, information retrieval, and despeckling.

Mr. Di Simone was awarded a prize for the Best Master Thesis in Remote Sensing by the IEEE South Italy Geoscience & Remote Sensing Chapter in 2015.

Antonio Iodice (S'97–M'00–SM'04) was born in Naples, Italy, in 1968. He received the Laurea degree (*cum laude*) in electronic engineering and the Ph.D. degree in electronic engineering and computer science from the University of Naples "Federico II," Naples, in 1993 and 1999, respectively.

In 1995, he was with the Research Institute for Electromagnetism and Electronic Components, Italian National Council of Research (IRECE-CNR), Naples, and from 1999 to 2000, he was with Telespazio S.p.A., Rome, Italy. From 2000 to 2004, he was a Research Scientist with the Department of Electronic and Telecommunication Engineering, University of Naples "Federico II." He is currently a Professor of electromagnetics with the Department of Electrical Engineering and Information Technology, University of Naples "Federico II." He has been involved as a Principal Investigator or a Coinvestigator in several projects funded by the European Union (EU), Italian Space Agency (ASI), Italian Ministry of Education and Research (MIUR), Campania Regional Government, and private companies. He is the author or coauthor of about 300 papers, of which about 70 were published on refereed journals and the others on proceedings of international and national conferences. His main research interests are in the field of microwave remote sensing and electromagnetics: modelling of electromagnetic scattering from natural surfaces and urban areas, simulation and processing of synthetic aperture radar signals, and electromagnetic propagation in urban areas.

Prof. Iodice is the Chair of the IEEE South Italy Geoscience and Remote Sensing Chapter. He received the "Sergei A. Schelkunoff Prize Paper Award" from the IEEE Antennas and Propagation Society for the best paper published in 2008 on the IEEE TRANSACTIONS ON ANTENNAS AND PROPAGATION in 2009.

Daniele Riccio (M'91–SM'99–F'14) was born in Naples, Italy. He received the Laurea degree (*cum laude*) in electronic engineering from the Università di Napoli Federico II, Naples, Italy, in 1989.

He is currently a Full Professor of electromagnetic theory and remote sensing with the Department of Electrical Engineering and Information Technology, University of Naples Federico II. He is a member of the Cassini Radar Science Team. He was a Research Scientist with the Italian National Council of Research at the Institute for Research on Electromagnetics and Electronic Components (1989–1994). He also was a Guest Scientist with the German Aerospace Centre (DLR), Munich, Germany (1994 and 1995), and taught, Ph.D. level, at the Universitat Politecnica de Catalunya, Barcelona, Spain (2006), and the Czech Technical University, Prague, Czech Republic (2012). He is a Principal Investigator for international research projects on exploitation of remote sensing data and design of synthetic aperture radars (SARs) and participates in technical committees of international symposia on electromagnetics and remote sensing. He is the Coordinator of the Ph.D. program in information technology and electrical engineering at the University of Napoli Federico II. He is an associate editor for some journals on remote sensing. He is the author of three books, including *Scattering, Natural Surfaces and Fractals* (2007), and over 350 papers. His research interests focus on microwave remote sensing, electromagnetic scattering, SAR with emphasis on sensor design, data simulation and information retrieval, and application of fractal geometry to remote sensing.

Prof. Riccio was the recipient of the 2009 Sergei A. Schelkunoff Transactions Prize Paper Award for the best paper published in year 2008 on the IEEE TRANSACTIONS ON ANTENNAS AND PROPAGATION.